OEP | Opto-Electronics Plus

Colourful cloud: active photoluminescent smokescreen for multi-wavelength non-line-of-sight channel establishment and enhancement

Yihua Hu[†*], Youlong Chen[†], Weijie Liu[†], Jingyin Tang, Hao Huang, Yuwei Chen, Yifan Ding, Xing Yang, Jingwen Zou, Tianrui Lin, Nuo Huang, Yushuang Zhang*, Chen Gong*

https://doi.org/10.29026/oep.2025.250001

OEP | Opto-Electronics Plus

Colourful cloud: active photoluminescent smokescreen for multi-wavelength non-line-of-sight channel establishment and enhancement

Yihua Hu, Youlong Chen, Weijie Liu, Jingyin Tang, Hao Huang, Yuwei Chen, Yifan Ding, Xing Yang, Jingwen Zou, Tianrui Lin, Nuo Huang, Yushuang Zhang and Chen Gong

Citation: Hu YH, Chen YL, Liu WJ, et al. Colourful cloud: active photoluminescent smokescreen for multi-wavelength non-line-of-sight channel establishment and enhancement. *Opto-Electronics Plus* **1**, 250001(2025).

https://doi.org/10.29026/oep.2025.250001

Received: 28 April 2025; Accepted: 27 June 2025; Published online: 4 July 2025

Related articles

Generation of lossy mode resonances (LMR) using perovskite nanofilms

Dayron Armas, Ignacio R. Matias, M. Carmen Lopez-Gonzalez, Carlos Ruiz Zamarreño, Pablo Zubiate, Ignacio del Villar, Beatriz Romero

Opto-Electronic Advances 2024, **7**(2): 230072 doi: 10.29026/oea.2024.230072

Observation of polaronic state assisted sub-bandgap saturable absorption

Li Zhou, Yiduo Wang, Jianlong Kang, Xin Li, Quan Long, Xianming Zhong, Zhihui Chen, Chuanjia Tong, Keqiang Chen, Zi-Lan Deng, Zhengwei Zhang, Chuan-Cun Shu, Yongbo Yuan, Xiang Ni, Si Xiao, Xiangping Li, Yingwei Wang, Jun He

Opto-Electronic Advances 2025, **8**(6): 240312 doi: 10.29026/oea.2025.240312

OEP Opto-Electronics Plus
www.oejournal.org/oep

Article
July 2025, Vol. 1, No. 1

DOI: 10.29026/oep.2025.250001

Open Access

Colourful cloud: active photoluminescent smokescreen for multi-wavelength non-line-of-sight channel establishment and enhancement

Yihua Hu[1,3*†], Youlong Chen[1,3†], Weijie Liu[2†], Jingyin Tang[2], Hao Huang[1,3], Yuwei Chen[3], Yifan Ding[2], Xing Yang[1,3,4], Jingwen Zou[1,3], Tianrui Lin[2], Nuo Huang[2], Yushuang Zhang[1,3,4]* and Chen Gong[2]*

Abstract: Non-line-of-sight (NLOS) optical wireless scattering communication, a solution for broader optical communication scenarios, is vulnerable to challenges in complex medium environments, simultaneous multiple terminals, and interference with strong pertinence. Here, we have developed an innovative photoluminescent smokescreen based on inorganic perovskite with reconfigurable optical field to facilitate NLOS multi-channel establishment and signal propagation enhancement. Accordingly, the smokescreen should exhibit configurable emission wavelength, high emission efficiency, excellent floatability, high stability and low biotoxicity. We propose an encapsulated $CsPbBr_3$ nanocrystal tunable aerogel technology under aqueous atmospheric pressure, and evaluate its performance through indoor/outdoor experiments. The experimental results prove the feasibility of NLOS optical propagation enhancement and indication with fabricated materials. Specifically, ultraviolet (UV) light (266 nm) is projected onto the smokescreen and down-converted to two wavelengths in the blue (488 nm) and green (529 nm) spectrum, forming a tri-wavelength signal propagation channel and visualising the incident region as a colourful cloud. The light reception enhancement for UV light, blue light and green light reaches two, twenty, and ten-fold, respectively. The performance gain brought by the wavelength conversion is shown for two types of daily-use glasses. The proposed paradigm will significantly facilitate the development of optical communication and sensing in NLOS areas.

Keywords: smokescreen; perovskite; photoluminescence; NLOS channel; optical communication

Introduction

Due to absorption and scattering effects, smokescreens normally impede line-of-sight (LOS) optical propagation[1,2]. These detection-blocking properties can be advantageous in protecting certain critical objects, obscuring vital movements, and reducing our capabilities in optical communication and sensing. Conversely, the optical scattering enhancement effect of smokescreens allows to establish a NLOS communication link between mobile terminals without stringent alignment requirements between the transmitter and receiver. Previous studies reveal that UV wireless light is highly suitable for local area NLOS optical wireless communication, resulting from its advantages of high bandwidth and "solar-blind" negligible background radiation[3–5]. However, NLOS UV wireless communication is vulnerable to challenges in long distances, expansive areas, complex medium environments, simultaneous multiple terminals, and interference with strong pertinence[6,7]. In order to establish a more reliable and robust optical communication link, it is imperative to explore innovative techniques to augment the scattering optical intensity[8]. The active smokescreen's scattering enhancement effect can be leveraged by actively releasing the smokescreen on the UV optical propagation path, thereby increasing the scattered light intensity as a secondary light source[9]. However, invisible propagation paths need to be visualized to indicate the scattering region, which will facilitate the pointing of

Received: 28 April 2025
Accepted: 27 June 2025
Published online: 4 July 2025

[1]State Key Laboratory of Pulsed Power Laser Technology, Hefei 230037, China; [2]University of Science and Technology of China, Hefei 230027, China; [3]Advanced Laser Technology Laboratory of Anhui Province, Hefei 230037, China; [4]Jianghuai Advance Technology Center, Hefei 230061, China.
† These authors contributed equally to this work
*Correspondence: YH Hu, E-mail: skl_hyh@163.com; YS Zhang, E-mail: yszhang@hnu.edu.cn;
C Gong, E-mail: cgong821@ustc.edu.cn

receivers.

To achieve the desired effect, nano inorganic perovskite materials are chosen due to their high absorption coefficient, low exciton binding energy, and long carrier diffusion length[10,11]. Numerous studies have highlighted the use of halide perovskite quantum dots as an effective optoelectronic component for optical devices[12,13]. Inorganic perovskite quantum dots of $CsPbX_3$ exhibit ultra-stable. stimulated emission with a tunable wavelength and cost-effective preparation[14]. Improving crystallization is another way to boost the performance of the material. Increasing the grain size and slowing down the crystallization can be achieved by different strategies such as solvent engineering[15–17], annealing engineering[18,19] and additive engineering[20]. The majority of $CsPbBr_3$ is synthesized in a toxic organic phase, which is not conducive to stable storage[21,22], so the preparation of a more stable solid powder is more conducive to the formation of smokescreen. The grain size of $CsPbBr_3$ significantly influences the peak of photoluminescence (PL). By strategically designing its grain size, an adjustable photoluminescence wavelength can be achieved. Additionally, the narrow full width at half maximum (FWHM) of $CsPbBr_3$ is advantageous for realizing multi-wavelength optical propagation[23–25]. We have designed a special smokescreen that employs a strategy of encapsulating $CsPbBr_3$ with molecular sieves[26–28] to achieve stable performance and dual photoluminescence wavelengths. This design can be utilized as a relay communication repeater. Consequently, the active photoluminescent smokescreen's attenuation of LOS optical propagation can create a configurable optical transmission environment, thereby facilitating NLOS high-speed optical propagation enhancement and indication. Here, visible wavelength lights can be emitted upon the delicate design and fabrication of smokescreens using fluorescent nanomaterials, which indicate the scattering region that the receiver should point to. Similarly, excited light on other wavelengths can generate additional light propagation for more complex optical communication, such as multi-channel communications. The above innovative paradigm for active smokescreen is shown in Fig. 1(e). Intense UV light is projected onto a released smokescreen composed of the specially designed nanomaterial. The intensity of the scattered UV light can be increased by the smokescreen, thereby expanding the coverage area for more reliable and robust communication. The visible light emitted from the smokescreen visually represents the scattering region, enabling the receiver to more easily direct its focus towards higher UV and other wavelength signal directions. Furthermore, the visible light can propagate through certain media, such as water and glass, with significantly less power attenuation than that of the UV signal. This could potentially facilitate Non-Line-of-Sight (NLOS) optical communication in a broader range of scenarios.

Herein, we have designed novel $CsPbBr_3$@molecular sieves and $CsPbBr_3$@molecular sieves@SiO_2 structures, achieving mass production of powder materials. Leveraging their superior PL properties, we have successfully utilized these materials to create special smokescreens, which facilitate NLOS multi-channel establishment and signal propagation enhancement in the UV (266 nm) and visible bands (488 and 532 nm).

Results

Principle of colourful cloud

Here Fig. 1(a) illustrates a digital image captured under natural light, as well as the operational status of the active smokescreen designed to facilitate the establishment and enhancement of multi-wavelength Non-Line-of-Sight (NLOS) channels. The incident UV light excites the electrons of the smokescreen material to an excited state, as illustrated in Fig. 1(d). Following electron relaxation, these electrons revert to their ground state, resulting in the emission of light at visible wavelengths. As depicted in Fig. 1(e), the active smokescreen is aerial sprayed, creating a colourful cloud effect when illuminated with UV light. To achieve long range detection in the model, an optimized optical detection system needs to be designed to receive weak fluorescent scattering signals

Preparation and characterization of smokescreen materials

Firstly, porous molecular sieve structures are prepared using the atmospheric pressure method as precursors for the blue-emitting material $CsPbBr_3$@Molecular Sieve and the green-emitting material $CsPbBr_3$@Molecular Sieve@SiO_2. This simple approach facilitates mass production and endows the materials with superior floatability. Specifically, Tetraethyl Orthosilicate (TEOS) is hydrolysed and orderly aggregated around the template Cetyltrimethylammonium Bromide (CTAB) through electrostatic interaction to form a framework, resulting in a uniform mesoporous structure of 6.4716 nm after sintering (as evidenced by Scanning electron microscope (SEM), High-angle annular dark field-scanning transmission electron microscopy (HAADF-STEM) images, nitrogen physisorption isotherms, and pore size distribution curve of the molecular sieves, shown in Fig. S1-1). The hollow and porous structure enhances floatability in air [29], ensuring the stability of the NLOS channel and providing additional binding sites for $CsPbBr_3$. Simultaneously, it effectively prevents damage from water and acidic media in the air. The thermogravimetric (TA) curve in Fig. S1-2 reveals that the molecular sieves have undergone a typical three-weight loss during sintering (Fig. S1-2)[30]. Secondly, a simple atmospheric pressure hydrothermal method is employed to synthesize the $CsPbBr_3$@Molecular Sieves based on molecular sieves as the blue emission (488 nm) material. Figure 1(b) and Fig. S1-3 show the TEM and high-resolution TEM (HRTEM) images

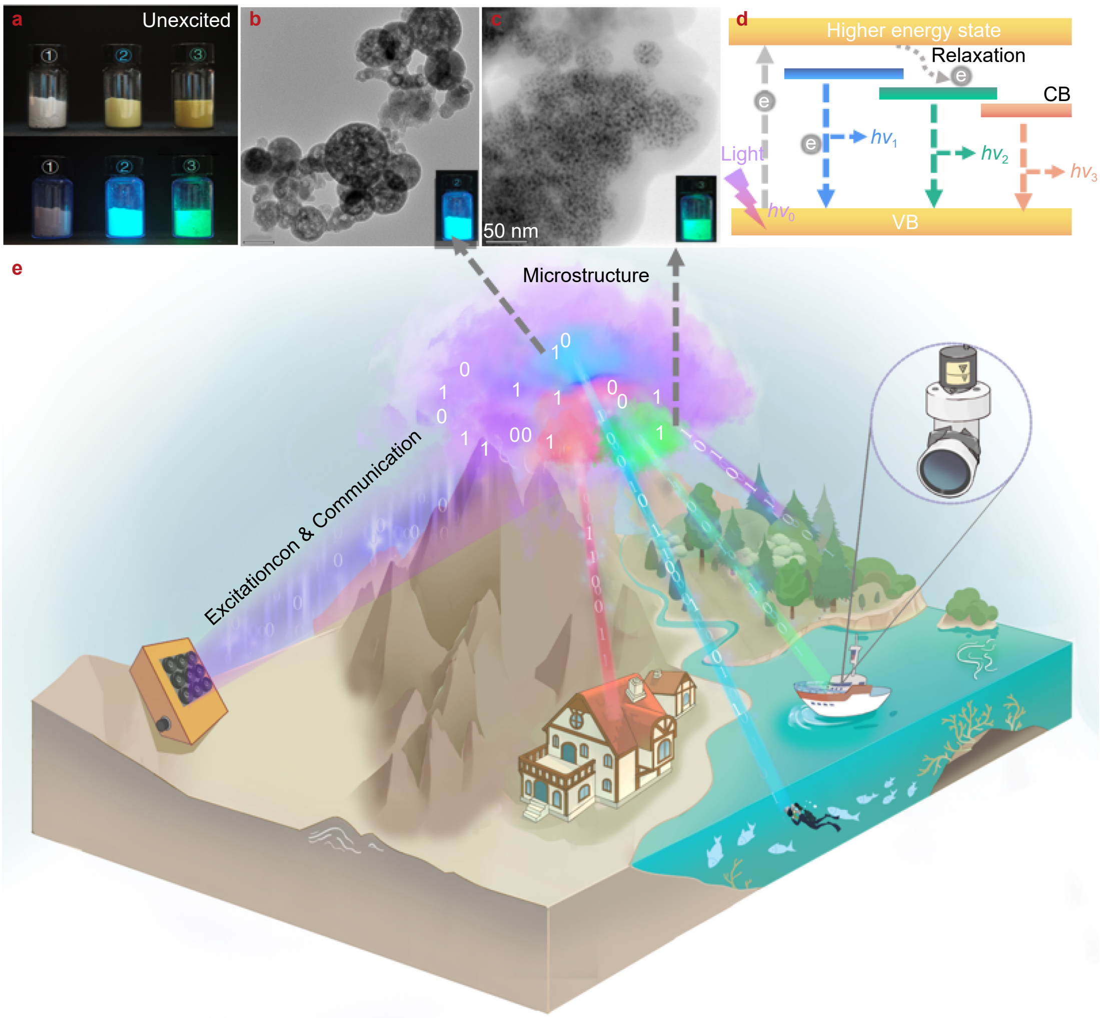

Fig. 1 | The model of multi-wavelength NLOS channel establishment and enhancement and physical properties of smokescreen materials. (**a**) The digital image of ① Molecular Sieves, ② $CsPbBr_3$@Molecular Sieves and ③ $CsPbBr_3$@Molecular Sieves@SiO_2 under natural light and wide illumination light source of 266 nm. (**b**) The transmission Electron Microscope (TEM) image of $CsPbBr_3$@Molecular Sieves. (**c**) The scanning transmission electron microscopy (STEM) brightfield image of $CsPbBr_3$@Molecular Sieves@SiO_2. (**d**) The schematic diagram of smokescreen material luminescence. (**e**) The Schematic of multi-wavelength NLOS channel establishment and enhancement, where the smokescreen can enhance the scattered UV signal intensity, visualize the scattering region and emit other propagation wavelengths.

of the $CsPbBr_3$@molecular sieves. $CsPbBr_3$ NCs effectively occupy pore sites of the molecular sieves (Fig. S1-3)[30], leading to a reduction in specific surface area and pore size (Tab. S1 and Fig. S1-1d). The significant change in the internal specific surface area suggests that $CsPbBr_3$ NCs are primarily located within the pores rather than adsorbed on the surface of molecular sieves. The HAADF-STEM image and corresponding elemental mappings of $CsPbBr_3$ @molecular sieves, as shown in Fig. S1-4, indicate a uniform distribution of Cs, Pb, and Br elements within the molecular sieves. Subsequently, $CsPbBr_3$@Molecular Sieves@SiO_2, a material that emits green light (529 nm), is synthesized from $CsPbBr_3$@Molecular Sieves via an atmospheric pressure hydrothermal method. Figure 1(c), Fig. S1-5, and Fig. S1-6 present the STEM brightfield, HRTEM, and HAADF-STEM images of $CsPbBr_3$@molecular sieves @SiO_2. The SiO_2, derived from the hydrolysis of APTES, encapsulates the $CsPbBr_3$@molecular sieves tightly, leading to a reduction in specific surface area and pore volume, with micropores nearly disappearing (Tab. S1 and Fig. S1-1d). The Cs, Pb, and Br elements are confined solely within the molecular sieves, not extending into the outer silica layer (Fig. S1-5 and S1-6). The presence of SiO_2 induces a template confinement effect, providing a more expansive space for the growth of $CsPbBr_3$ within the molecular sieve[28]. This allowed for the formation of larger $CsPbBr_3$ nanocrystals (NCs). The encapsulation of the molecular sieves not only stabilizes the materials but also reduces the toxicity of $CsPbBr_3$. We employ normal human respiratory system cells to gauge the potential toxicity of materials on the human body. According to the United States Pharmacopeia toxicity grading methodology, the cytotoxicity evaluation indicates that the smokescreen materials display a toxicity level of 0 at a material concentration of 8 mg/L, signifying its low-toxic nature (Fig. S1-9). The surface element composition and ion state of the nanocomposites are detected by X-ray photoelectron spectroscopy (XPS). Figure 2(a) illustrates that both $CsPbBr_3$@Molecular Sieves and $CsPbBr_3$@Molecular Sieves@SiO_2 display a comprehensive spectrum of elements including C, Si, O, Cs, Pb, and Br. More specifically, the primary peaks for $CsPbBr_3$@Molecular Sieves are situated at 103.3 eV (Si 2p), 532.94 eV (O 1s), 725.2 eV and 739.2 eV (Cs 3d), 143.2 and 138.6 eV (Pb 4f), 68.8 eV and 69.8 eV (Br 3d) (Fig. 2(b) and Fig. S2-1).[31] Based on our previous research[32], The green-emitting material, $CsPbBr_3$@Molecular Sieves@SiO_2, exhibits a smaller bandgap, as evidenced by the redshift in emission (Fig. 2(c)), compared to the blue-emitting material, $CsPbBr_3$@Molecular Sieves. The narrowing of the FWHM of PL spectrum for $CsPbBr_3$@Molecular Sieves@SiO_2 suggests an increase in the purity of light emission. This shows that the incorporation of silica improves crystal quality, which is consistent with the Time-resolved photoluminescence (TRPL) measurements and the surface binding energy shift of about 0.5 eV (Fig. 2(b) and Fig. S2-1b-d).

To validate the indication, multi-channel establishment, and signal propagation enhancement capabilities of powder materials in communication, we characterize the PL spectra and TRPL of $CsPbBr_3$@Molecular Sieves and $CsPbBr_3$@Molecular Sieves@SiO_2. As shown in Fig. 2(c-d), the material exhibits PL characteristics with a central wavelength of 487 nm and 529 nm, aligning with the narrowband filter (488±5nm and 532nm±5nm) used in subsequent light reception experiments. The FWHM are 36 nm and 22 nm, respectively, without overlap. The working state of the powder material within the smokescreen box is illustrated in Fig. S1-8. The material's colour under a broad illumination light source of 266 nm is depicted in Fig. 1(a), demonstrating superior blue and green PL with high emission efficiency. As shown in Fig. 2(d-e), TRPL is conducted to further investigate the material's defect density and channel enhancement characteristics. The average lifetime of $CsPbBr_3$@Molecular Sieves (3.89 ns) is significantly lower than that of $CsPbBr_3$@Molecular Sieves@SiO_2 (6.61 ns). The increase in the lifetime of the fast component is attributed to changes in the radiation recombination rate of intrinsic excitation. The increase in the lifetime of the slow component is attributed to the reduction of the non-radiation recombination process associated with surface traps.[33,34] As the wrapping silica thickens, the average and slow lifetime of $CsPbBr_3$@Molecular Sieves@SiO_2 gradually increase (Fig. 2(e)), indicating a decrease in the defect state and the number of non-radiating composite channels. The reduction in defect state density leads to higher crystalline quality of the grown material. Further, it improves the luminescence properties of the material, which is consistent with the reduction in the FWHM of PL in Fig. 2(c). The time-resolved

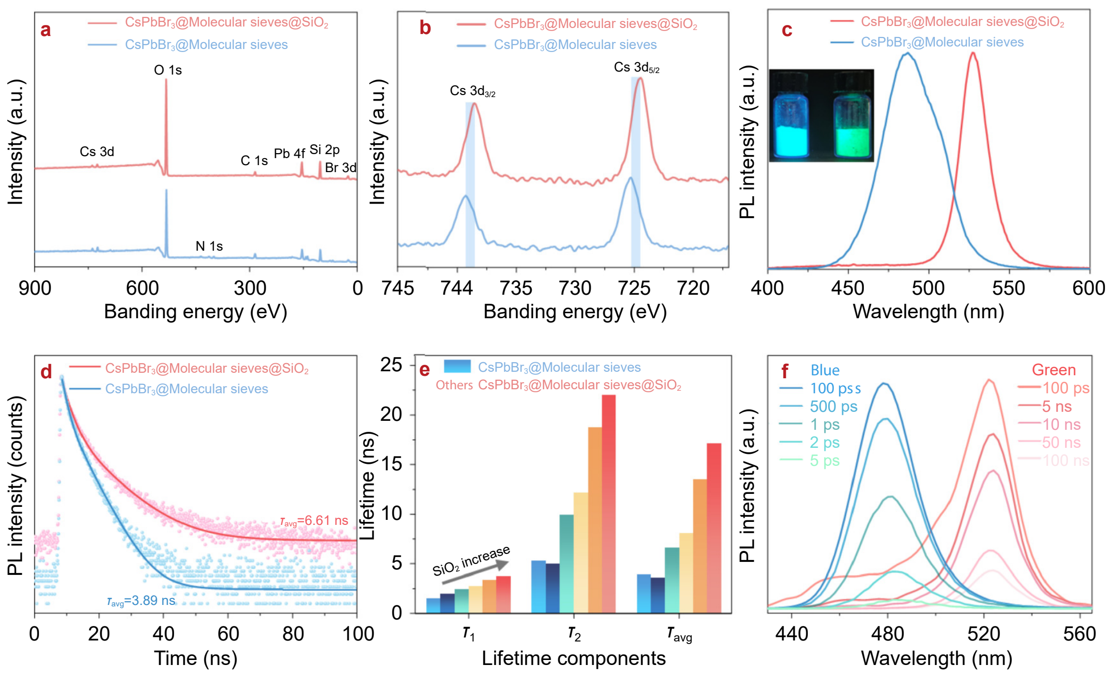

Fig. 2 | The electronic and optical properties of materials. (**a**) The XPS survey and (**b**) binding energies correspond to the Cs 3d of $CsPbBr_3$@Molecular Sieves and $CsPbBr_3$@Molecular Sieves@SiO_2. (**c**) The PL spectra of $CsPbBr_3$@Molecular Sieves and $CsPbBr_3$@Molecular Sieves@SiO_2. Inset: the image of two materials under a wide illumination light source of 266 nm. (**d**) TRPL of $CsPbBr_3$@Molecular Sieves and $CsPbBr_3$@Molecular Sieves@SiO_2. (**e**) Short, long, and average lifetime components of $CsPbBr_3$@Molecular Sieves and $CsPbBr_3$@Molecular Sieves@SiO_2 with different SiO_2 thicknesses. (**f**) The time-resolved emission spectra of $CsPbBr_3$@Molecular Sieves and $CsPbBr_3$@Molecular Sieves@SiO_2.

emission spectra (Fig. 2(f) and Fig. S2-3) reveal that the emission wavelength remains consistent at both nanoseconds and picoseconds time scales for $CsPbBr_3$@Molecular Sieves, which matches the requirements for stable high-speed communication.

Indoor tests

An indoor test has been conducted in a dark room to verify the light intensity enhancement capacity of the fluorescent material. We utilize two types of fluorescent materials, centered at 488 nm (blue) and 529 nm (green) wavelengths, respectively. The blue fluorescent material, $CsPbBr_3$@ Molecular Sieves, and the green fluorescent material, $CsPbBr_3$@Molecular Sieves@SiO_2 are mixed in equal proportions, hereafter referred to as the mixture. This mixture is subjected to indoor testing under NLOS conditions, as illustrated in Fig. 3(a), where the presence of walls obstructed the direct light path. Three photomultipliers (PMT) detectors (UV one at 266 nm, blue one at 488 nm, and green one at 532 nm) are adopted to measure the light intensity from the NLOS link using a UV light source, which is obscured by three optical filters with corresponding center lengths. As detailed in Fig.3(b), Groups 1 and 2 are used to measure ambient noise levels, Groups 3 and 4 operated with the UV light source without a smokescreen, and Groups 5-8 incorporated both the UV light source and the fluorescent mixture. Fig. 3(c-h) present the original signal waveforms of 4000 sampling points in various scenarios at 1Mbps transmission rate and 100 MSaps sampling rate, equivalent to 40 symbols. Before the smokescreen emission, as shown in Fig. 3(c-e), only the detector can receive the 266 nm NLOS UV light. At this moment, the average number of detected photoelectrons for the signal components at 266 nm, 488 nm, and 532 nm are 5.4562, 0.0134, and 0.6534, respectively, while the average numbers of detected photoelectrons for the background radiation components at 266 nm, 488 nm, and 532 nm are 0.7106, 0.0048 and 0.2838, respectively. Comparing Fig. 3(c-e) with Fig. 3(f-h), it can be observed that the mixture material enhances the scattering of UV photons and successfully radiates the visible light component at 488 nm and 532 nm. Post-emission, the average number of detected photoelectrons for the signal components is 11.7308 at 266 nm, 0.2736 at 488 nm, and 6.6762 at 532 nm. The corresponding photoelectron counts for the noise components are 1.7186 at 266 nm, 0.0372 at 488 nm, and 1.2054 at 532 nm. Under NLOS conditions, the enhancements achieved were 2.1-fold at 266 nm, 20.4-fold at 488 nm, and 10.2-fold at 532 nm, demonstrating the substantial improvement in light intensity due to the smokescreen.

Outdoor tests

We have previously tried NLOS under different light intensity conditions, and the test intensity under dark room environment is about 30 times that under strong light intensity background (sunlight) (see Tab. S8-1 for relevant test results). In order to more intuitively characterize the feasibility of colour cloud communication capabilities, we conducted NLOS tests in outdoor environments with low light intensity. The outdoor test is conducted at Zipeng Hill (Longitude 117.006592, Latitude 31.712114), Hefei, from 9 PM to 12 PM in the spring. As illustrated in Fig. 4(a-b), the transmitter and receiver are placed on either side of a corner without a LOS link. The scattering angle between the transmission and reception links is approximately 70 degrees. The transmitter consists of a high-power UV LED with an optical power of 1W and a full divergence angle of 7 degrees. Three PMT detectors are situated on the opposite side of the corner, equipped with UV, blue and green optical filters to detect the light at wavelengths of 266 nm, 488 nm and 532 nm, respectively. Two lens hoods are placed on the receiving optics, the blue and green light detectors, to mitigate background radiation. Fig. 4(d-e) illustrate the blue and green light excitation when a mixture of smokescreen material is sprayed onto the corner. It is observed that the excitations in the blue and green spectrum are discernible with a sprayed mixed smokescreen.

Ten groups of tests are performed, as shown in Fig. 4(e). The detailed experimental setup and test data are shown in Section S6 of the Supplementary Material. The UV light intensity increases two to three times with the sprayed smokescreen. With lens hoods, the blue and green light intensity amplifies to three to ten times the background radiation. The captured waveforms of the UV PMT, without and with smokescreen, are presented in Fig. 4(f-i), respectively, demonstrating a noticeable enhancement in light intensity. Moreover, the captured waveforms of the 488 nm and 532 nm wavelengths without smokescreen are illustrated in Fig. 4(g-h), respectively, and with smokescreen are shown in Fig. 4(j-k), respectively.

The potential communication performance at wavelengths of 488 nm and 532 nm can be predicted based on spreading spectrum. The signals at a wavelength of 488 nm are spread with factors 512, 1024 and 2048, and those at a wavelength of 532 nm are spread with factors 32, 64 and 128. These detailed results are shown in Fig. S6-2 in the Supplementary Material. It is evident that as the quantum efficiency increases to 0.9, the residue Bit Error Rate (BER) can fall below the correction threshold (3.8×10^{-3}) under spreading factors 512 and 32 for blue and green light respectively. Moreover, it can be predicted that after propagating the illustrated two types of glasses, the number of photons for green light will be more than 10 times of that for UV light, as inferred from the transmittance curve and the variation of refractive index across different wavelengths presented in Fig. S6-3. Such result demonstrates the performance enhancement conferred by wavelength conversion in specific transmission media, thereby potentially improving the adaptability of optical wireless communication in complex media. At the same time, we also carry out real-time communication under strong and weak light environment based on colourful cloud, and realize channel

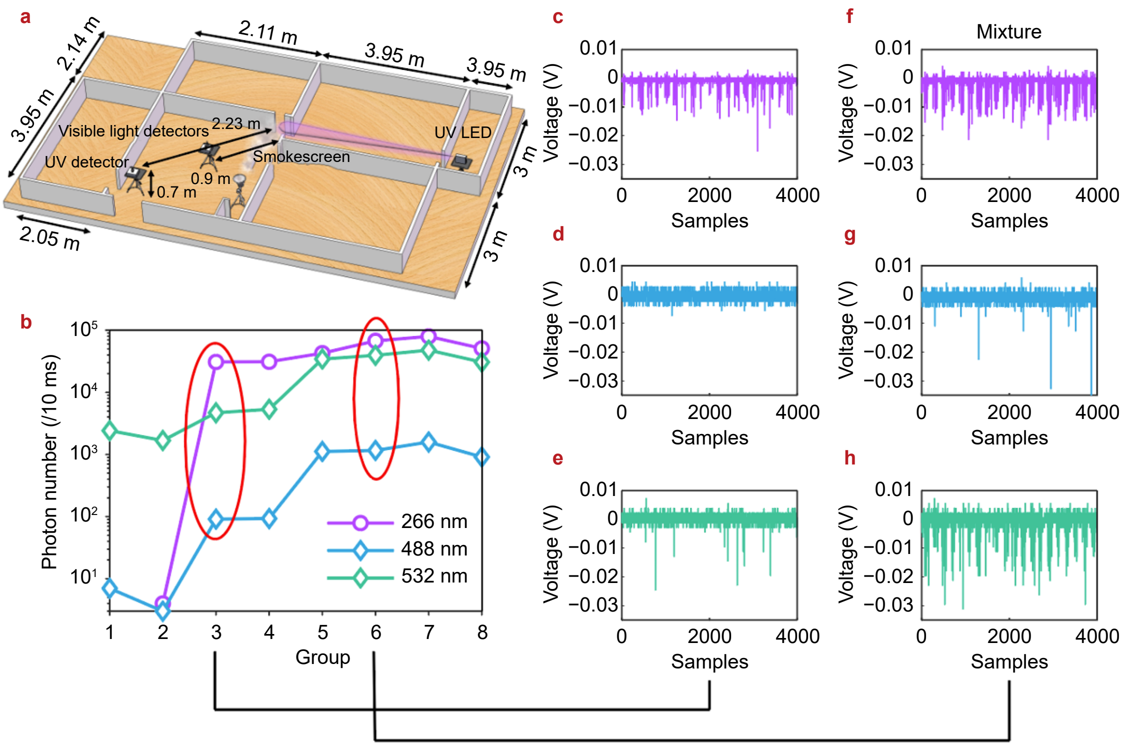

Fig. 3 | Indoor Application experimental setup and result. (**a**) Schematic of experimental setup. The left part of the diagram shows the UV and visible light detectors, and the right part shows the UV light source. The light emitted by the UV LED is received by the UV detector after transmission through the atmospheric channel, and the visible light component excited by the smokescreen (prepared by mixing $CsPbBr_3$@Molecular Sieves and $CsPbBr_3$@Molecular Sieves@SiO_2 in a 1:1 ratio) is received by the visible light detectors. All three detectors have filters corresponding to the central wavelength to eliminate interference outside the passband. (**b**) Photon counting results within 10 ms at 1 Mbps transmission and 100M sampling rates. (**c-e**) Photon reception levels of the three colours in the absence of smokescreen. (**f-h**) Photon reception levels of three colours with the sprayed smokescreen. The smokescreen can effectively enhance the scattering of UV photons, thus improving the reception level of the NLOS link and successfully exciting the visible light component of 488 nm and 532 nm.

establishment and information transmission with and without daily-use Glasses (see the Section S7). These results demonstrate reliable communication link and demonstrate the advantages of colour cloud communication in the environment where UV light does not pass.

Discussion and outlook

We have developed a special smokescreen composed of inorganic perovskite fluorescent nanocrystals encapsulated within molecular sieves using a tunable aerogel technology under aqueous atmospheric pressure, which can be "configurable" to establish and enhance the NLOS channel communication. The fabricated artificial smokescreen materials can enhance Rayleigh scattering and be excited to generate visible light by incident UV light. Two types of powder nanomaterials have been synthesized with centre down-converted wavelengths of blue (488 nm) and green (529 nm), when excited by incident UV light (266 nm). We have conducted two proof-of-concept experiments in indoor and outdoor fields. In the indoor tests, the scattering intensity of UV light significantly increases, and the visible light receivers detect both blue and green light at the photon-counting level. In the outdoor tests, the smokescreen materials enhance the UV scattering intensity, serve as a visible scattering region indicator for the receiver-side PMT detector pointing, and create other transmission wavelengths. The performance gain brought by the wavelength conversion is shown for certain transmission media (Fig. S6-3). The innovative paradigm utilizing the active smokescreen holds great potential for future developments in optical communication and sensing in NLOS areas.

Materials and methods

Materials

Caesium bromide (CsBr, 99.9%), lead (II) bromide ($PbBr_2$, 99.0%), and 3-Aminopropyltriethoxysilane (APTES, 99%) are purchased from Macklin.

Synthesis of Molecular Sieves

Firstly, 16.9g CTAB were fully dissolved in 500 mL ultrapure water and slowly drip in 50 mL of TEOS. Adjust the pH of the mixture to 10.7 using an ammonium hydroxide solution. Filter and wash repeatedly with ultrapure water after stirring for 2 h. Dry the mixture at 80 °C and grind. Secondly, heat the powder at 300 °C for 2 h. Lastly, heat the powder again at 720 °C for 6 h and thoroughly grind it to obtain the molecular sieves.

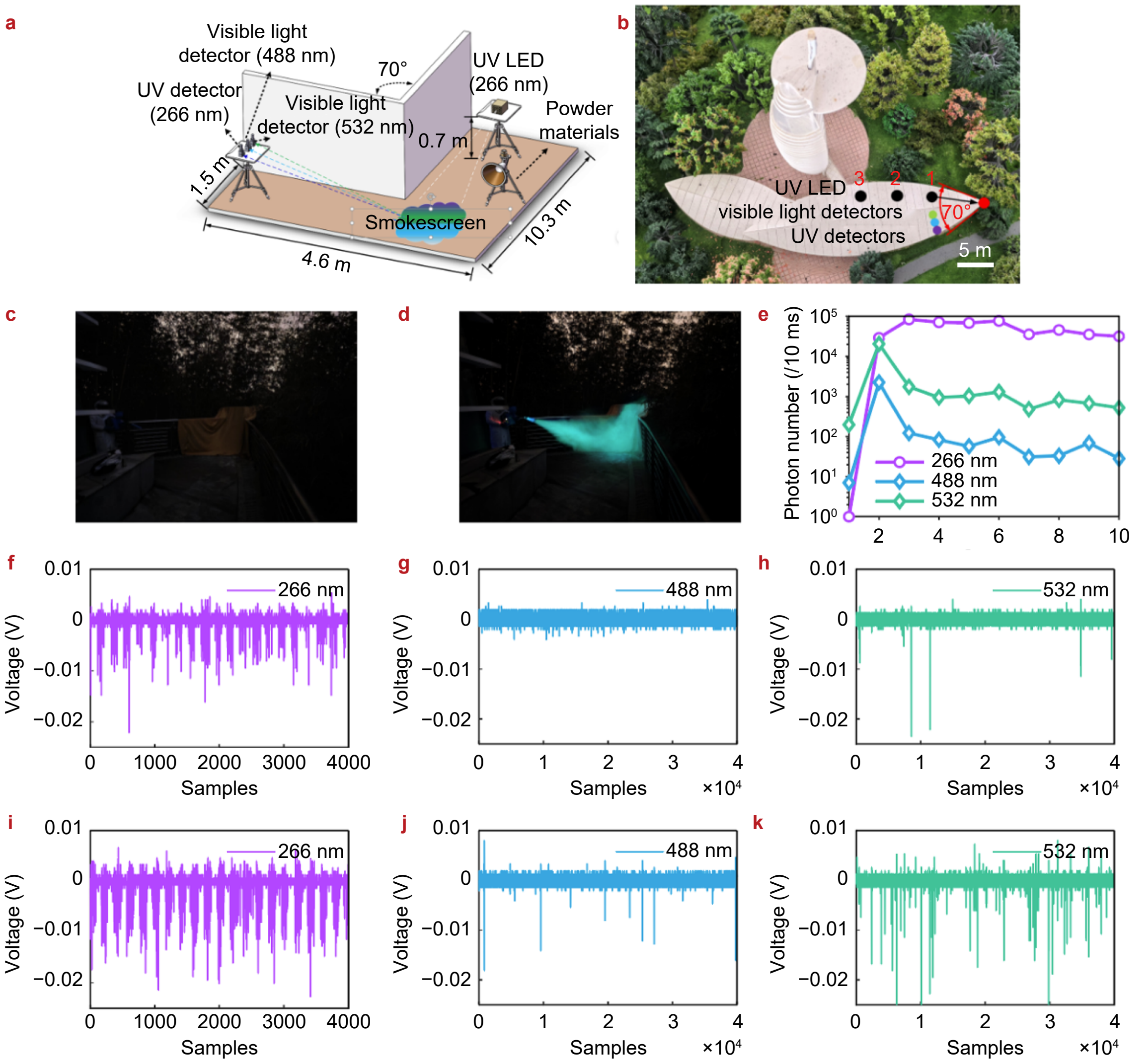

Fig. 4 | Outdoor experimental setup and result. (**a**) Schematic of experimental setup. The LOS links between the UV light source and detectors are blocked. (**b**) Top view of the experimental environment. (**c-d**) Visible light radiated in the absence of smokescreen and spraying the smokescreen (prepared by mixing $CsPbBr_3$@Molecular Sieves and $CsPbBr_3$@Molecular Sieves@SiO_2 in a 1:1 ratio). A mixture smokescreen can emit significant visible light signals, serving as an indicator for the receiver's direction. (**e**) The three-colour photon counting results within 10 ms at 1 Mbps transmission rate and 100M sampling rate. 266 nm, 488 nm and 532 nm photon reception levels: (**f-h**) without smokescreen; (**i-k**) with smokescreen. Up to 2.88 times UV signal strength enhancement can be observed when aligned with the smokescreen.

Synthesis of $CsPbBr_3$@Molecular Sieves

Typically, 0.25 mM CsBr and 0.25 mM $PbBr_2$ were fully dissolved in 40 mL ultrapure water at 80 °C and stirred at 1000 rpm for 1 h. 0.7246 g molecular sieves were added to the mixture solution and stirred at 1000 rpm for 5 h. Dry the reactants at 80 °C and heat them at 600 °C for 10 min.

Synthesis of $CsPbBr_3$@Molecular Sieves@SiO_2

Firstly, 0.25 mM CsBr and 0.25 mM $PbBr_2$ were fully dissolved in 40 mL ultrapure water at 80 °C and stirred at 1000 rpm for 1 h. Secondly, 0.7246 g molecular sieves were added to the mixture solution and stirred at 1000 rpm for 40 min. Thirdly, 1 mL of APTES was added to the mixture solution and stirred at 1000 rpm for 5 h. Lastly, dry the reactants at 80 °C.

Characterizations

The TEM, HRTEM, HAADF-STEM, EDS and STEM brightfield images were performed using a Thermofisher FEI Talos F200XG2 microscope operated at an accelerating voltage of 200 kV. The SEM image was performed using a ZEISS Sigma 300 microscope operated at an accelerating voltage of 3 kV. An Edinburgh FS5 spectrophotometer assessed PL, time-resolved emission spectrum, and TERL. TA curve was carried out using Netzsch STA 449 F3. The surface areas and pore properties were analysed using Micromeritics ASAP 2460. The XPS spectra were measured using a Thermo Scientific ESCALAB Xi+, and the X-ray diffraction (XRD) studies were performed using a Bruker D8 Advance.

On the transmitter side, an on-off keying (OOK) signal is generated offline and loaded into an arbitrary waveform generator (AWG, 33600A Keysight) for modulation of UV LED to generate an optical signal. The optical signal drives the UV LED with a central wavelength of 266 nm and a peak optical power of 1W. After transmission through the atmospheric channel, the optical signal is received by three photomultiplier tubes. PMT1 is of model Hamamatsu R13096 with a 266nm bandpass filter. PMT2 and PMT3 are model Hamamatsu CR315 with 488 nm and 532 nm bandpass filters, respectively. The power supply of PMTs is all provided by a direct-current power supply (DC, Rigol DP832A). The signals received by each PMT were sampled by an oscilloscope (OSC, Keysight MSOX6004A) to record the real-time waveforms, and finally, the pulse counting was processed on a computer.

References

1. Ijaz M, Ghassemlooy Z, Pesek J et al. Modeling of fog and smoke attenuation in free space optical communications link under controlled laboratory conditions. *J Lightwave Technol* **31**, 1720–1726 (2013).
2. Rahman Z, Shah TN, Zafaruddin SM et al. Performance of dual-hop relaying for OWC system over foggy channel with pointing errors and atmospheric turbulence. *IEEE Trans Veh Technol* **71**, 3776–3791 (2022).
3. Gong C, Xu ZY. Non-line of sight optical wireless relaying with the photon counting receiver: a count-and-forward protocol. *IEEE Trans Wirel Commun* **14**, 376–388 (2015).
4. Zou DF, Gong C, Wang K et al. Characterization on practical photon counting receiver in optical scattering communication. *IEEE Trans Commun* **67**, 2203–2217 (2019).
5. Jiang ZM, Gong C, Xu ZY. Achievable rates and signal detection for photon-level photomultiplier receiver based on statistical non-linear model. *IEEE Trans Wirel Commun* **18**, 6015–6029 (2019).
6. Wang ZW, Li XY, Pu MB et al. Vectorial-optics-enabled multi-view non-line-of-sight imaging with high signal-to-noise ratio. *Laser Photonics Rev* **18**, 2300909 (2024).
7. Zhao ZB, Zhang Q, Li XY et al. High-resolution non-line-of-sight imaging based on liquid crystal planar optical elements. *Nanophotonics* **13**, 2161–2172 (2024).
8. Guo YH, Lei YS, Pu MB et al. Vectorial digitelligent optics for high-resolution non-line-of-sight imaging. *Engineering* **45**, 70–78 (2025).
9. Tang JY, Ding YF, Lin TR et al. Ultraviolet communication with a large scattering angle via artificial agglomerate fog. *Opt Express* **31**, 23149–23170 (2023).
10. Kaplan AEK, Krajewska CJ, Proppe AH et al. Hong–Ou–Mandel interference in colloidal $CsPbBr_3$ perovskite nanocrystals. *Nat Photonics* **17**, 775–780 (2023).
11. Zaffalon ML, Cova F, Liu MM et al. Extreme γ-ray radiation hardness and high scintillation yield in perovskite nanocrystals. *Nat Photonics* **16**, 860–868 (2022).
12. Zhao L, Zhou Y, Shi ZF et al. High-yield growth of $FACsPbBr_3$ single crystals with low defect density from mixed solvents for gamma-ray spectroscopy. *Nat Photonics* **17**, 315–323 (2023).
13. Chen CS, Chen JX, Han HC et al. Perovskite solar cells based on screen-printed thin films. *Nature* **612**, 266–271 (2022).
14. Jiang YZ, Sun CJ, Xu J et al. Synthesis-on-substrate of quantum dot solids. *Nature* **612**, 679–684 (2022).
15. Sidhik S, Wang YF, De Siena M et al. Deterministic fabrication of 3D/2D perovskite bilayer stacks for durable and efficient solar cells. *Science* **377**, 1425–1430 (2022).
16. Park J, Kim J, Yun HS et al. Controlled growth of perovskite layers with volatile alkylammonium chlorides. *Nature* **616**, 724–730 (2023).
17. Morad V, Stelmakh A, Svyrydenko M et al. Designer phospholipid capping ligands for soft metal halide nanocrystals. *Nature* **626**, 542–548 (2024).
18. Chen XM, Lu WG, Tang JL et al. Solution-processed inorganic perovskite crystals as achromatic quarter-wave plates. *Nat Photonics* **15**, 813–816 (2021).
19. Hou JW, Chen P, Shukla A et al. Liquid-phase sintering of lead halide perovskites and metal-organic framework glasses. *Science* **374**, 621–625 (2021).
20. Xue JJ, Wang R, Chen XH et al. Reconfiguring the band-edge states of photovoltaic perovskites by conjugated organic cations. *Science* **371**, 636–640 (2021).
21. Pan L, Liu ZF, Welton C et al. Ultrahigh-flux X-ray detection by a solution-grown perovskite $CsPbBr_3$ single-crystal semiconductor detector. *Adv Mater* **35**, 2211840 (2023).
22. Polimeno L, Coriolano A, Mastria R et al. Room temperature polariton condensation from whispering gallery modes in $CsPbBr_3$ microplatelets. *Adv Mater* **36**, 2312131 (2024).
23. Zhu CL, Nguyen T, Boehme SC et al. Many-body correlations and exciton complexes in $CsPbBr_3$ quantum dots. *Adv Mater* **35**, 2208354 (2023).
24. Brennan MC, Veghte DP, Ford BR et al. Photolysis of mixed halide perovskite nanocrystals. *ACS Energy Lett* **8**, 2150–2158 (2023).
25. Dutta SK, Peng LC, Hudait B et al. Halide perovskite cluster precursors: a paradigm for obtaining structure- and color-tunable light-emitting nanocrystals. *ACS Energy Lett* **7**, 3177–3186 (2022).
26. Cui JY, Zhang ZQ, Yang LF et al. A molecular sieve with ultrafast adsorption kinetics for propylene separation. *Science* **383**, 179–183 (2024).
27. Fan MT, Xu SJ, An B et al. Bimetallic aluminum- and niobium-doped MCM-41 for efficient conversion of biomass-derived 2-methyltetrahydrofuran to pentadienes. *Angew Chem Int Ed* **61**, e202212164 (2022).
28. Polshettiwar V. Dendritic fibrous nanosilica: discovery, synthesis, formation mechanism, catalysis, and CO_2 capture–conversion. *Acc Chem Res* **55**, 1395–1410 (2022).
29. Rossi C, Scarfiello R, Brescia R et al. Exploiting the transformative features of metal halides for the synthesis of $CsPbBr_3$@SiO_2 core–shell nanocrystals. *Chem Mater* **34**, 405–413 (2022).
30. Damyanova S, Pawelec B, Arishtirova K et al. MCM-41 supported PdNi catalysts for dry reforming of methane. *Appl Catal B Environ* **92**, 250–261 (2009).
31. Wang JR, Jia G, Kong HX et al. Highly efficient luminescence and enhanced stability of nanocomposites by encapsulating perovskite quantum dots in defect-related luminescent silica nanospheres. *Appl Surf Sci* **591**, 153258 (2022).
32. Chen YL, Hu YH, Ma L et al. Self-assembled $CsPbBr_3$ quantum dots with wavelength-tunable photoluminescence for efficient active jamming. *Nanoscale* **14**, 17900–17907 (2022).
33. Stranks SD, Eperon GE, Grancini G et al. Electron-hole diffusion lengths exceeding 1 micrometer in an organometal trihalide perovskite absorber. *Science* **342**, 341–344 (2013).
34. Chen HT, Guo AQ, Zhu J et al. Tunable photoluminescence of $CsPbBr_3$ perovskite quantum dots for their physical research. *Appl Surf Sci* **465**, 656–664 (2019).

Acknowledgements

This work was supported by the National Natural Science Foundation of China (61871389, 62304256), the College of Electronic Engineering (KY22C213, KY24A204, KY25A005), the State Key Laboratory of Pulsed Power Laser Technology (KY21C604), the Scientific Research Project of National University of Defense Technology under Grant (22-ZZCX-07), the Hefei Comprehensive National Science Center (KY23C502) and Hefei Comprehensive National Science Center and Jianghuai Advanced Technology Center.

Author contributions

YouLong Chen and Weijie Liu conceived of the initial idea, proposed the analytical strategy, and performed most of the experiments, with the guidance of YiHua Hu, Chen Gong and YuShuang Zhang. Jingyin Tang, Hao Huang, and Yuwei Chen assisted in the preparation of some materials. Yifan Ding, Tianrui Lin and Nuo Huang modified the manuscript. Xing Yang, Jingwen Zou, and Tianrui Lin wrote the manuscript with feedback from other authors.

Competing interests

The authors declare no competing financial interests.